Finite element model predictions of static deformation from dislocation sources in a subduction zone: Sensitivities to homogeneous, isotropic, Poisson-solid, and half-space assumptions

Timothy Masterlark

U.S. Geological Survey, Sioux Falls, South Dakota, USA

EROS Data Center, Science Applications International Corporation, Sioux Falls, South Dakota, USA

Received 6 November 2002; revised 1 August 2003; accepted 14 August 2003; published 22 November 2003.

[1] Dislocation models can simulate static deformation caused by slip along a fault. These models usually take the form of a dislocation embedded in a homogeneous, isotropic, Poisson-solid half-space (HIPSHS). However, the widely accepted HIPSHS assumptions poorly approximate subduction zone systems of converging oceanic and continental crust. This study uses three-dimensional finite element models (FEMs) that allow for any combination (including none) of the HIPSHS assumptions to compute synthetic Green's functions for displacement. Using the1995 M_w = 8.0 Jalisco-Colima, Mexico, subduction zone earthquake and associated measurements from a nearby GPS array as an example, FEM-generated synthetic Green's functions are combined with standard linear inverse methods to estimate dislocation distributions along the subduction interface. Loading a forward HIPSHS model with dislocation distributions, estimated from FEMs that sequentially relax the HIPSHS assumptions, yields the sensitivity of predicted displacements to each of the HIPSHS assumptions. For the subduction zone models tested and the specific field situation considered, sensitivities to the individual Poisson-solid, isotropy, and homogeneity assumptions can be substantially greater than GPS measurement uncertainties. Forward modeling quantifies stress coupling between the M_w = 8.0 earthquake and a nearby M_w = 6.3 earthquake that occurred 63 days later. Coulomb stress changes predicted from static HIPSHS models cannot account for the 63-day lag time between events. Alternatively, an FEM that includes a poroelastic oceanic crust, which allows for postseismic pore fluid pressure recovery, can account for the lag time. The pore fluid pressure recovery rate puts an upper limit of 10^{-17} m^2 on the bulk permeability of the oceanic crust. *INDEX TERMS:* 1242 Geodesy and Gravity: Seismic deformations (7205); 3230 Mathematical Geophysics: Numerical solutions; 3260 Mathematical Geophysics: Inverse theory; 7215 Seismology: Earthquake parameters; 7223 Seismology: Seismic hazard assessment and prediction; *KEYWORDS:* finite element models, pororelastic theory, static deformation, stress coupling, material properties, tectonic hazards

Citation: Masterlark, T., Finite element model predictions of static deformation from dislocation sources in a subduction zone: Sensitivities to homogeneous, isotropic, Poisson-solid, and half-space assumptions, *J. Geophys. Res.*, *108*(B11), 2540, doi:10.1029/2002JB002296, 2003.

1. Introduction

[2] A model is an approximation of a natural system. An acceptable degree of simplification depends on the desired accuracy of model predictions, the availability of constraining information, and the limitations of the modeling device or method. The reliability of model predictions depends on how well the model approximates the field situation [*Wang and Anderson*, 1982]. Consequently, selecting an appropriate model is an important consideration when conducting an analysis of static deformation caused by slip along a fault. A dislocation along a surface can simulate the release of elastic strain accumulation (slip) along a fault and account for observed deformation caused by earthquakes [e.g., *Hutton et al.*, 2001] and creep events [e.g., *Dragert et al.*, 2001]. Relatively simple models of a dislocation embedded in a homogeneous, isotropic, Poisson-solid half-space (HIPSHS) are the standard for predicting static deformation caused by slip along a fault [*Cohen*, 1999]. Dislocation source parameters determined from multiple types of static deformation data such as GPS displacements, interferometric synthetic aperture radar imagery, and surface offset measurements suggest that slip along a fault is not uniform and is best described as a distribution of dislocation sources [*Wald and Heaton*, 1994; *Pritchard et al.*, 2002; *Miyazaki et al.*, 2003]. The aim of this paper is to identify the sensitivities of

0148-0227/03/2002JB002296$09.00

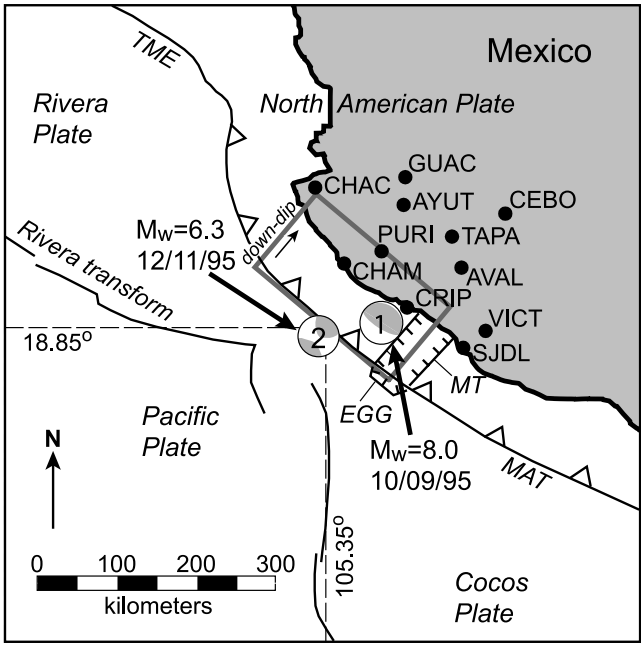

Figure 1. Reference map, west-central coast of Mexico. The M_w = 8.0 Jalisco-Colima earthquake (focal mechanism 1) ruptured a 220-km-long portion of the Middle America trench on 9 October 1995. An M_w = 6.3 event (focal mechanism 2) occurred on 11 December 1995, a few tens of kilometers to the southwest of the rupture zone. The spatial and temporal proximity of the two events suggest that they are coupled. The gray rectangle outlines the surface projection of the rupture. The black circles are the 11 GPS site locations. The location of the center of the intersection of the rupture and the free surface is 18.85°N and 105.35°W. Tectonic features MAT, TME, MT, and EGG are the Middle America trench, Tres Marias escarpment, Manzanillo trough, and El Gordo graben, respectively.

dislocation and displacement predictions to each of the HIPSHS assumptions for subduction zone models.

[3] Finite element models (FEMs) are constructed to simulate slip along a fault in a subduction zone, using the 1995 M_w = 8.0 Jalisco-Colima, Mexico, earthquake as an example. FEM configurations include the combined suite of HIPSHS assumptions as well as configurations that systematically relax the individual assumptions. Deformation predictions from the various FEM configurations are compared to three-component displacement data from 11 GPS sites. This study (1) points out that models requiring HIPSHS assumptions poorly represent subduction zones; (2) illustrates a previously established method for computing synthetic Green's functions, using FEMs that do not require HIPSHS assumptions, for both forward and inverse models of static deformation due to dislocation sources; (3) demonstrates that displacement prediction errors, introduced by HIPSHS assumptions, can be severe; and (4) estimates the sensitivities of stress-coupling calculations to the HIPSHS assumptions.

[4] This study investigates the effects of the HIPSHS assumptions on a particular type of model commonly used to predict deformation and stress for subduction zones. The assumptions common to all the models in this study are linear elastic behavior, deformation driven entirely by dislocations (no remote loading), and no gravitational effects. The results of this study may be extended to estimate the significance of the HIPSHS assumptions in other subduction zone models, for which the above assumptions are appropriate. However, the relative importance of each HIPSHS assumption is ultimately dependent upon the particular model application. Other types of models exist, and the results of this study do not necessarily pertain to those models.

1.1. Jalisco-Colima Earthquake

[5] The 9 October 1995, M_w = 8.0 Jalisco-Colima earthquake ruptured the Rivera-North American plate subduction interface near the coast of Jalisco, Mexico (Figure 1). Significant recent earthquakes along this region of the Middle America trench occurred on 3 June 1932 (M_w = 8.2) and 8 June 1932 (M_w = 7.8) [*Singh et al.*, 1985]. Earthquake focal mechanisms for the 6 October 1995, M_w = 5.8 foreshock, the 9 October 1995, M_w = 8.0 main shock, and the 12 October 1995, M_w = 6.0 aftershock [*Escobedo et al.*, 1998] are consistent with thrusting at a depth of about 20 km in a direction rotated 10° counterclockwise from the trench-normal (N40°E) Rivera-North America convergence direction [*DeMets and Wilson*, 1997]. Seismogenic results suggest that the 1995 M_w = 8.0 event consisted of four shallow subevents, the first of which occurred near the northwest edge of the Manzanillo trough. The locations of the three following subevents indicate that the rupture propagated along the strike of the slipping portions of the subduction interface (the fault) to the northwest [*Escobedo*, 1998]. The 1995 M_w = 8.0 event occurred close enough to a GPS geodetic array to allow the study of both the coseismic and postseismic behavior of the event. Previous inversions of the coseismic displacement measurements from the 11 GPS sites (Table 1) suggest that two regions dominate the dislocation distribution along the fault. One is beneath the epicenter and the other is about 100 km northwest of the epicenter [*Melbourne et al.*, 1997; *Hutton et al.*, 2001; *Masterlark et al.*, 2001]. The "coseismic" GPS displacements are determined from measurements spanning an interval beginning 7 months before the earthquake and ending several days after the earthquake [*Hutton et al.*, 2001]. Therefore respective interseismic strain and postseismic deformation before and after the event contaminate the coseismic GPS data. This study ignores the contamination.

[6] On 11 December 1995, an earthquake swarm occurred a few tens of kilometers southwest of the M_w = 8.0 rupture. The swarm included an M_w = 6.3 main shock having a predominantly strike-slip focal mechanism (Table 2) in accord with historical focal mechanisms [*DeMets and Stein*, 1990] and the principal stresses of the M_w = 8.0 earthquake. The spatial and temporal proximity of the swarm to the M_w = 8.0 earthquake suggests a causal relationship. However, the 63-day lag between the M_w = 8.0 earthquake and the subsequent swarm suggests a quasi-static [*Masterlark and Wang*, 2002] rather than a static-coupling mechanism.

1.2. Need for Improvement

[7] We can test the validity of a presupposed dislocation model by comparing predictions of deformation with observed data. Although direct observations of deformation at

Table 1. GPS Data[a]

GPS Site	Longitude, °W	Latitude,°W	u_{east}, m	1σ, m	u_{north}, m	1σ, m	u_{up}, m	1σ, m
AVAL	103.6840	19.4810	−0.1347	0.0083	−0.0718	0.0037	−0.0685	0.0174
AYUT	104.3740	20.1880	−0.1290	0.0133	−0.1760	0.0065	−0.1636	0.0330
CEBO	103.1610	20.0900	−0.0603	0.0114	−0.0305	0.0056	−0.0150	0.0261
CHAC	105.4290	20.3840	−0.0264	0.0108	−0.0879	0.0047	−0.0080	0.0253
CHAM	105.0840	19.5270	−0.4763	0.0087	−0.8432	0.0035	−0.2146	0.0174
CRIP	104.3330	19.0310	−0.2908	0.0034	−0.3802	0.0016	−0.0615	0.0074
GUAC	104.3540	20.5010	−0.0495	0.0101	−0.1158	0.0051	−0.0420	0.0254
PURI	104.6370	19.6650	−0.2730	0.0089	−0.4117	0.0040	−0.1016	0.0198
SJDL	103.6630	18.5770	0.0009	0.0093	−0.0010	0.0038	−0.0620	0.0204
TAPA	103.7970	19.8310	−0.1257	0.0162	−0.1088	0.0062	−0.0236	0.0341
VICT	103.3960	18.7680	−0.0230	0.0078	0.0094	0.0034	−0.0606	0.0164

[a]From *Hutton et al.* [2001].

the Earth's surface are commonly available, it is difficult to directly observe slip along a buried fault. Because quantified estimations of slip along a fault can have far-reaching implications, substantial effort has gone into the development of inverse prediction models that strive to accurately estimate dislocation source distributions, a proxy for slip along a fault, based on observed deformational data and presupposed HIPSHS models [e.g., *Cervelli et al.*, 2001; *Miyazaki et al.*, 2003]. Although it is well known that some of the HIPSHS assumptions can introduce enormous prediction errors [*Eberhart-Phillips and Stuart*, 1992; *Masterlark et al.*, 2001; *Wald and Graves*, 2001], little attention is typically given to the implications of the presupposed HIPSHS models. Dislocation distributions determined from superb observed data and elaborate inverse schemes may be precise but are most likely inaccurate if the presupposed model is not a good representation of the field situation, as is generally the case for HIPSHS models.

[8] Deviations from HIPSHS models are often rejected on the basis that the observed deformational data do not allow additional model complexity [*Bawden*, 2001]. Furthermore, analytical solutions for displacement due to a dislocation source in an HIPSHS are readily available and computationally inexpensive [*Okada*, 1992, and references therein]. Hence presupposed HIPSHS dislocation models underlie the vast majority of analyses of static deformation caused by slip along a fault. A flaw in this viewpoint is the existence of many types of data, other than direct displacement observations, that require deviations from and complexities beyond the HIPSHS assumptions.

[9] The half-space assumption implies that the top of the problem domain, the free surface, is flat. The total relief of a subduction zone, from the trench to the volcanic arc, can be several kilometers. Topographic effects can have a significant impact on static displacement [*Williams and Wadge*, 2000; *Tinti and Armigliato*, 2002] and stress [*Wang and He*, 1999] predictions. Digital elevation and bathymetry models having at least 1-km spatial resolution are readily available and easily implemented in FEMs.

[10] The Poisson-solid assumption (Poisson's ratio $\nu = 0.25$) is not representative of crustal rocks. Poisson's ratio for common crustal rocks can be $0.1 < \nu < 0.4$ [*Turcotte and Schubert*, 1982], although the range for the bulk representation of the crust is $0.25 < \nu < 0.32$ [*Christensen*, 1996].

[11] Pore fluids exist in the upper crust to a depth of several kilometers [*Nur and Walder*, 1992, and references therein]. Although the porosity of crystalline basement rocks is only a few percent at most, the poroelastic behavior can be significant under the loading conditions associated with large earthquakes [*Masterlark et al.*, 2001; *Bosl and Nur*, 2002; *Masterlark and Wang*, 2002]. The choice of material properties to represent the upper crust must therefore account for the poroelastic state of the system. Undrained conditions prevail during relatively short times following an instantaneous event of slip along a fault (an earthquake) because the static stress transfer is faster than the response of pore fluid flow. Undrained elastic constants reflect a relatively stiff behavior with respect to their drained counterparts. The relationship between drained and undrained values for Poisson's ratio, ν and ν_u respectively, is

$$\nu = \frac{3\nu_u - \alpha B(1+\nu_u)}{3 - 2\alpha B(1+\nu_u)}, \quad \nu_u = \frac{3\nu + \alpha B(1-2\nu)}{3 - \alpha B(1-2\nu)}, \qquad (1)$$

where B is Skempton's coefficient and α is the Biot-Willis parameter [*Wang*, 2000]. The drained and undrained values of Poisson's ratio for Westerly granite, for which elastic properties are commonly used in deformational modeling [*Kaufman and Royden*, 1994; *Masterlark and Wang*, 2000, 2002; *Masterlark et al.*, 2001; *Parsons*, 2002], are 0.25 and 0.34, respectively [*Wang*, 2000]. Displacements predicted for a dislocation along a rectangular surface using the equations given by *Okada* [1992] can differ by more than 10% for drained versus undrained conditions. For static coseismic deformation (undrained conditions), a Poisson-solid is a poor material property assumption even if (drained) Poisson's ratio is 0.25.

Table 2. Focal Mechanisms[a]

Event	M_w	M_o, dyne/cm	Latitude, °N	Longitude, °W	Plane	Strike	Dip	Rake
9 October 1995	8.0	1.15×10^{28}	19.34	104.8	fault	302	9	92
					node	120	81	90
11 December 1995	6.3	3.4×10^{25}	18.84	105.75	fault	175	82	17
					node	83	74	171

[a]Harvard CMT, http://www.seismology.harvard.edu/CMTsearch.html.

[12] Geologic observations [*Vauchez et al.*, 1998], shear wave splitting [*Russo and Silver*, 1994; *Yang et al.*, 1995; *Marson-Pidgeon et al.*, 1999; *Hartog and Schwartz*, 2000], P_n anisotropy [*Smith and Ekström*, 1999], and laboratory measurements [*Ismaïl and Mainprice*, 1998; *Godfrey et al.*, 2000; *Christensen et al.*, 2001] indicate that the elastic properties of the lithosphere are generally not isotropic. Mechanisms accounting for observed elastic anisotropy include periodic layering of isotropic materials near the Earth's surface, aligned microcracks in the brittle upper crust, lattice preferred orientations in the lower crust and upper mantle, and oriented inclusions having seismic properties in contrast to those of the surrounding material in the lower crust and upper mantle [*Meissner et al.*, 2002].

[13] The material properties of the Earth's lithosphere are not homogeneous. Unconsolidated materials at shallow depths are relatively compliant, whereas upper mantle rocks are relatively rigid. Significant vertical and the lateral contrasts between material properties in the crust, particularly across faults [*Rubin and Gillard*, 2000] and in plate boundary zones [*Holbrook et al.*, 1996], are well known. These contrasts are readily apparent near convergent plate boundaries, where the relatively stiff oceanic crust of the downgoing slab comes in contact with the relatively compliant overriding continental crust along the subduction interface. Others have previously demonstrated the sensitivities of deformation predictions due to dislocations for problem domains having homogeneous versus heterogeneous material property distributions [*Eberhart-Phillips and Stuart*, 1992; *Masterlark et al.*, 2001; *Wald and Graves*, 2001].

2. Method

2.1. Finite Element Model (FEM): Configurations and Assumptions

[14] FEMs in this study are constructed with the commercially available finite element code "ABAQUS" (version 6.2, Hibbet, Karlsson, & Sorensen, Inc., available at http://www.hks.com). This code allows for the heterogeneous distributions of anisotropic material properties and appropriate geometric relationships required for simulating coseismic, transient postseismic, and interseismic deformational phenomena associated with a subduction interface. The code solves for displacement (u) and coupled displacement and pore fluid pressure (u, P) for a problem domain having a combination of elastic and poroelastic properties. Expressed in index notation, the three governing equations for the elastic materials are

$$G\nabla^2 u_i + \frac{G}{(1-2\nu)}\frac{\partial^2 u_k}{\partial x_i \partial x_k} = -F_i, \tag{2}$$

and the four governing equations for the poroelastic materials are

$$G\nabla^2 u_i + \frac{G}{(1-2\nu)}\frac{\partial^2 u_k}{\partial x_i \partial x_k} = \alpha\frac{\partial P}{\partial x_i} - F_i \tag{3}$$

$$\alpha\frac{\partial \varepsilon_{kk}}{\partial t} + S_\varepsilon\frac{\partial P}{\partial t} = \frac{k}{\mu_f}\nabla^2 P + Q, \tag{4}$$

where G is the shear modulus, F is a body force, ε_{kk} is the volumetric strain, S_ε is the constrained storage coefficient, k is permeability, μ_f is the pore fluid viscosity, and Q is a fluid source term [*Wang*, 2000].

[15] Six FEMs are constructed to test the sensitivity of deformation predictions to each of the HIPSHS assumptions. The first FEM, model A, simulates the HIPSHS assumptions and serves as the reference model. Prediction differences between model A and the four other models that sequentially relax the HIPSHS assumptions identify relative sensitivities to each of the assumptions. The sixth model includes none of the HIPSHS assumptions. Table 3 summarizes the configurations of the six FEMs (models A through F).

[16] Some of the configuration specifications are common to all models. The simulated three-dimensional problem domain (Figure 2) includes a 40-km-thick continental crust of the North American plate [*Pardo and Suárez*, 1995] separated into 16- and 24-km-thick upper and lower crust layers. The oceanic crust of the subducting Rivera plate has a thickness of 6 km. The upper mantle extends from the base of the crust of both plates to a depth of about 200 km. The trench-parallel direction of the problem domain measures 1800 km. The North American and Rivera plates extend 800 and 600 km, respectively, in the horizontal trench-normal directions. The top of the problem domain is a free surface. Positions for the 11 nodes nearest to the GPS sites are adjusted to correspond to the simulated GPS site locations. The base and lateral boundaries have zero-displacement specifications. Sensitivity tests of alternative boundary configurations indicate the chosen configuration approximates zero displacement at infinity for the lateral and bottom boundaries.

[17] The convex interface separating the simulated Rivera and North American plates is a deformable contact surface consisting of node-pairs from the respective plates. The simulated fault, centered in the trench-parallel direction, consists of 143 contact node-pairs spaced approximately 20 and 10 km apart in the respective along-strike and downdip directions of the fault. Downdip spacing is reduced to about 5 km for the two rows of node-pairs nearest to the simulated rupture trace. The cross-sectional depth (d) of the subduction interface is related to the horizontal projection of the downdip distance (x) in kilometers, such that $d = Ax^n$, where $A = 0.029$, and $n = 1.55$ [*Hutton et al.*, 2001]. The two lithospheric plates are welded together along the downdip and along-strike extensions of the slipping portion of the interface. Kinematic constraints, which specify that all three corresponding displacement components for nondislocating node-pairs are equivalent, impose the welded conditions.

[18] A single set of drained elastic material properties is specified for the entire problem domain of the first FEM (model A), which simulates HIPSHS assumptions. Drained elastic properties determined from laboratory experiments for Westerly granite [*Wang*, 2000] satisfy the Poisson-solid assumption. The second FEM, model B, relaxes the half-space assumption and includes topography. The vertical positions of the nodes along the free surface of the continental crust are interpolated from a 1-km digital elevation model (D. A. Hastings et al., Global Land One-Kilometer Base Elevation (GLOBE) Digital Elevation Model, version 1.0, available at http://www.ngdc.noaa.gov/seg/

Table 3. Configurations of Models A–F

	Rheology	Elastic Constants
		Model A
Synthetic Green's function matrix: $\mathbf{G}_A$ Dislocation source: $\mathbf{m}_A$ Free surface: flat		
Upper continental crust, lower continental crust, oceanic crust, mantle	elastic	Westerly granite [*Wang*, 2000] G = 15 GPa ν = 0.25
		Model B
Synthetic Green's function matrix: $\mathbf{G}_B$ Dislocation source: $\mathbf{m}_B$ Free surface: topography		
Upper continental crust, lower continental crust, oceanic crust, mantle	elastic	Westerly granite [*Wang*, 2000] G = 15 GPa ν = 0.25
		Model C
Synthetic Green's function matrix: $\mathbf{G}_C$ Dislocation source: $\mathbf{m}_C$ Free surface: flat		
Upper continental crust, lower continental crust, oceanic crust, mantle	elastic	Westerly granite (undrained) [*Wang*, 2000] G = 15 GPa ν = 0.34
		Model D
Synthetic Green's function matrix: $\mathbf{G}_D$ Dislocation source: $\mathbf{m}_D$ Free surface: flat		
Upper continental crust, lower continental crust, oceanic crust, mantle	elastic	stiffness tensor,[a] GPa [*Godfrey et al.*, 2000] 53.62 14.08 11.41 0 0 0 14.08 53.62 11.41 0 0 0 11.41 11.41 43.95 0 0 0 0 0 0 14.63 0 0 0 0 0 0 19.77 0 0 0 0 0 0 19.77
		Model E
Synthetic Green's function matrix: $\mathbf{G}_E$ Dislocation source: $\mathbf{m}_E$ Free surface: flat		
Upper continental crust	elastic	Westerly granite [*Wang*, 2000] G = 15 Gpa ν = 0.25
Lower continental crust	elastic	Westerly granite [*Wang*, 2000] G = 15 Gpa ν = 0.25
Oceanic crust	poroelastic	Hanford basalt [*Wang*, 2000] G = 21 Gpa ν = 0.30 ν_u = 0.31 B = 0.12
Mantle	elastic	[*Turcotte and Schubert*, 1982] G = 60 Gpa ν = 0.25
		Model F
Synthetic Green's function matrix: $\mathbf{G}_F$ Dislocation source: $\mathbf{m}_F$ Free surface: topography		
Upper continental crust	poroelastic	Westerly granite [*Wang*, 2000] G = 15 Gpa ν = 0.25 ν_u = 0.34 B = 0.85

Table 3. (continued)

	Rheology	Elastic Constants					
Lower continental crust	elastic	stiffness tensor, GPa [*Godfrey et al.*, 2000]					
		116.99	30.73	24.89	0	0	0
		30.73	116.99	24.89	0	0	0
		24.89	24.89	95.90	0	0	0
		0	0	0	31.93	0	0
		0	0	0	0	43.13	0
		0	0	0	0	0	43.13
Oceanic crust	poroelastic	Hanford basalt [*Wang*, 2000]					
		G = 21 Gpa					
		ν = 0.30					
		ν_u = 0.31					
		B = 0.12					
Mantle	elastic	stiffness tensor, GPa [*Ismaïl and Mainprice*, 1998]					
		192.07	69.92	72.35	0.21	−0.04	0.10
		69.92	237.08	73.47	−0.31	0.25	0.61
		72.5	73.47	208.75	−0.30	0.23	−0.28
		0.21	−0.31	−0.03	72.55	0.01	0.38
		−0.04	0.025	0.23	0.01	63.28	0.09
		0.10	0.61	−0.28	0.38	0.09	68.5

[a]Scaled such that $K = K^*$, see equation (5).

topo/globe.shtml, 1999). The third FEM, model C, relaxes the Poisson-solid assumption. A Poisson's ratio of 0.34, the undrained value for the Poisson's ratio of Westerly granite [*Wang*, 2000], is specified for the homogeneous problem domain. Model C is equivalent to FEM_B given in the work of *Masterlark et al.* [2001]. The fourth FEM, model D, relaxes the isotropy assumption. A transversely isotropic stiffness tensor, M, is specified for the entire problem domain. In order to make a valid comparison between predictions from models A and D, the stiffness tensor, determined from laboratory experiments on Chugach phyllite [*Godfrey et al.*, 2000], is scaled such that the generalized bulk modulus, K^*, of the transversely isotropic stiffness tensor [*Cheng*, 1997] is equivalent to the bulk modulus, K, of the isotropic material specified in model A.

$$K = K^* = \frac{M_{iijj}}{9}. \tag{5}$$

The tensor is rotated into the model coordinate system such that the compliant (slow) axis is aligned with the horizontal trench-normal direction [e.g., *Currie et al.*, 2001; *Smith and Eckström*, 1999]. The fifth FEM, model E, relaxes the homogeneity assumption and is similar to FEM_C given in the work of *Masterlark et al.* [2001]. However, model E includes an elastic upper continental crust having the material properties specified for the entire problem domain of model A. Model E represents regional-scale heterogeneity of a subduction zone. Trench-parallel and lateral heterogeneities other than those of the subduction interface are not considered.

[19] The sixth FEM, model F, includes none of the HIPSHS assumptions. The top (free surface) of the continental crust is the same as that of model B. The oceanic crust and continental crust have poroelastic parameters for Hanford basalt and Westerly granite, respectively [*Wang*, 2000]. The lower continental crust is an elastic material having the transversely isotropic stiffness tensor for Chugach phyllite [*Godfrey et al.*, 2000]. The compliant axis of the tensor is aligned in the horizontal trench-normal direction. The upper mantle is an elastic material having fully

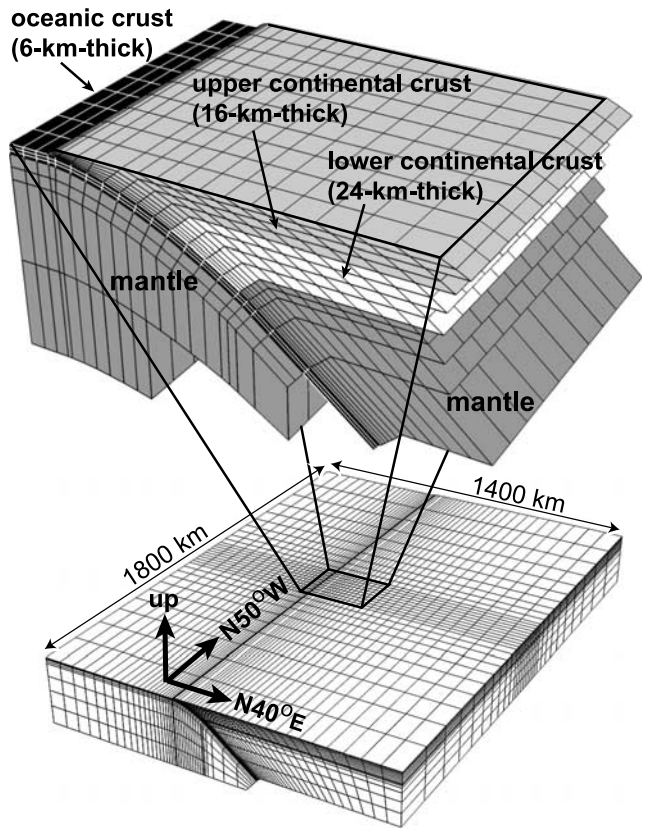

Figure 2. FEM configuration. The problem domain (lower portion) is tessellated into 29,624 nodes and 24,750 three-dimensional brick elements and approximates the geometry of a subducting slab and the overriding continental lithosphere. A local region surrounding the slipping part of the subduction interface is extracted in the upper part.

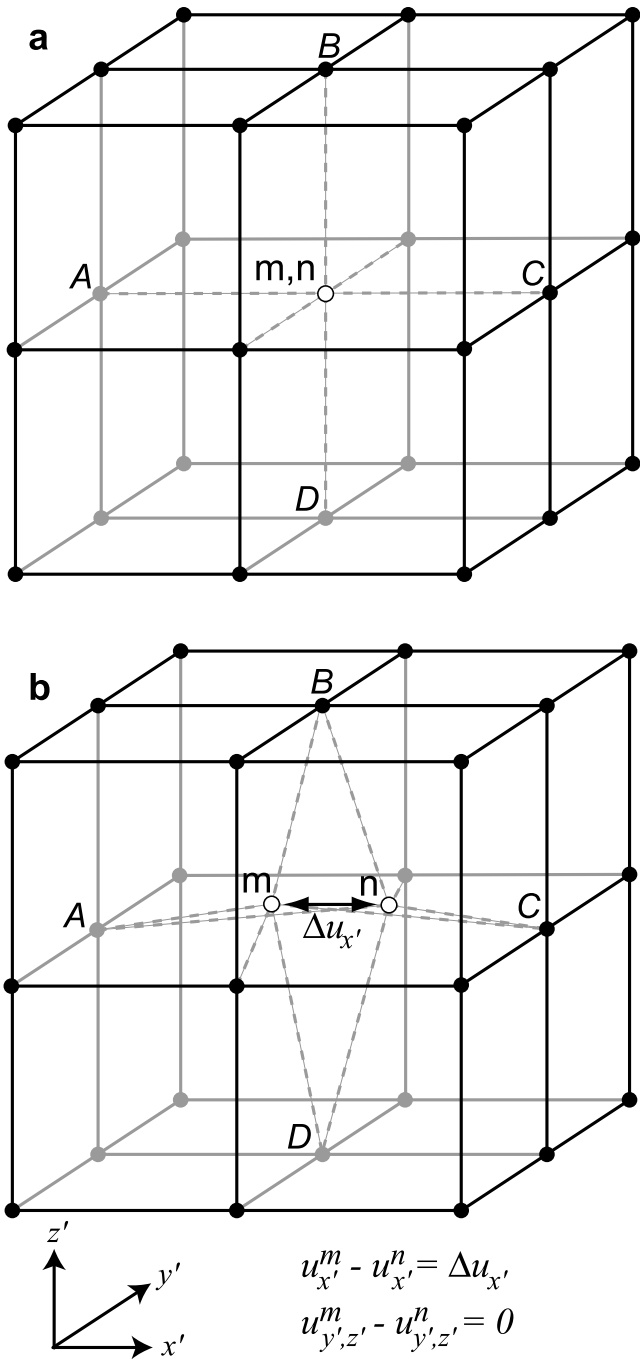

Figure 3. Dislocation of a node-pair. (a) The schematic FEM mesh includes a node-pair consisting of initially collocated nodes *m* and *n* on fault patch ABCD. (b) The static dislocation is implemented by imposing the kinematic constraints shown at the bottom, where the dislocation vector, $\Delta\mathbf{u}_{x'}$, is parallel x'. Three-dimensional translation of the dislocation vector is allowed, hence ABCD is a deformable surface. In this schematic, the mesh is distorted beyond the applicability of infinitesimal strain. However, dislocations in the actual FEMs used in this study are less than 0.1% of the characteristic length of the elements.

anisotropic elastic properties derived from laboratory experiments on rocks having fabrics similar to those of mantle rocks [*Ismaïl and Mainprice*, 1998]. The stiffness tensor is rotated into the model coordinate system such that the fast axis is trench parallel and the slow axis is horizontally trench normal, in accord with field-based shear wave splitting and P_n anisotropy observations [*Smith and Eckström*, 1999, and references therein]. This model also allows for fully coupled transient poroelastic behavior. The bulk permeability of the continental crust is 10^{-15} m^2 [*Masterlark and Wang*, 2002]. The bulk permeability of the oceanic crust is a calibration parameter discussed in the stress-coupling analysis. Model F is an attempt to account for our knowledge of the regional-scale mechanical structure of a subduction zone.

[20] The FEMs solve for incremental changes with respect to a reference state that occurs an instant before the dislocation [*Wang*, 2000]. The initial conditions are equilibrium $(u, P)|_{t=0} = 0$. Additional fluid-flow specifications are required for models E and F. The free-surface and lateral boundaries of the poroelastic layers have zero excess fluid pressure, and the bases of these layers have zero fluid-flow specifications. For model F, fluid flow is allowed across the interface between the poroelastic oceanic and upper continental crust. This implies an isotropic permeability structure within the fault zone.

2.2. FEM-Generated Synthetic Green's Functions

[21] The forward solution for displacements due to a dislocation distribution in a linear mechanical system, which has a priori geometric and material property specifications, is a system of linear equations

$$\mathbf{Gm} = \mathbf{d}, \tag{6}$$

where **G** is the matrix of synthetic Green's functions for displacement (the data kernel), **m** is a vector of dislocations for node-pairs simulating fault slip, and **d** is the data vector of observed three-component GPS displacements (Table 1). Each coefficient $\mathbf{G}_{ij}$ is a displacement component at location *j* due to a unit dislocation of node-pair *i*. Dislocation distributions can be estimated from equation (6) with standard linear inverse methods. The matrix of synthetic Green's functions is calculated using a presupposed FEM, for which the HIPSHS assumptions are not required.

[22] The dislocation method for an internal boundary in a two-dimensional FEM introduced by *Smith* [1974] and used by others [e.g., *Williams and McCaffrey*, 2001] is extended for use in three-dimensional FEMs simulating both HIPSHS and non-HIPSHS assumptions, using the finite element code ABAQUS and kinematic constraints. The dislocation between a pair of nodes, initially occupying the same position, is a prescribed relative displacement between the nodes. These node-pairs deform freely in unison in the two directions orthogonal to the dislocation vector and deform freely in tandem in the direction parallel to the dislocation vector (Figure 3).

[23] The method is implemented through several steps. First, a dummy node not connected to any active elements in the problem domain is assigned to each of the active node-pairs. Second, corresponding node-pairs and dummy nodes are rotated into a local coordinate system so that one

of the coordinate axes (x') is aligned parallel to a dislocation vector and another (y') is normal to the fault surface. Third, the two displacement components orthogonal to the dislocation vector are constrained to be equivalent for both nodes in a pair. Fourth, a displacement specification for the corresponding dummy node and a linear kinematic constraint equation achieve the relative displacement between nodes in a pair. This method simulates a dislocation using a relative displacement along a fault and does not require corrections associated with other methods that specify the absolute displacement along a fault [*Tinti and Armigliato*, 2002]. The **G** matrix is constructed by sequentially imposing a unity dislocation for each node-pair and null dislocations for all other node-pairs along the fault. The FEM contains 143 node-pairs; therefore the construction of a **G** matrix requires 143 forward model runs for each model configuration. This method is a powerful tool for analyses of static deformation because it can calculate synthetic Green's functions for static displacement for problem domains having any combination (including none) of the HIPSHS assumptions.

[24] The dislocation distributions are estimated using the damped least squares (DLS) method. Damped smoothing constraints that minimize differences between neighboring dislocations [*Wald and Heaton*, 1994] append the relationship in equation (6). The diagonal of the weighting matrix [*Menke*, 1989], **w**, is constructed from the uncertainties given in Table 1. Correlations between the three displacement components of the GPS data are negligible [*Hutton et al.*, 2001]. The forward solution then takes the form

$$\begin{pmatrix} \mathbf{w}^{-1}\mathbf{G} \\ \beta\mathbf{L} \end{pmatrix} \mathbf{m} = \begin{pmatrix} \mathbf{w}^{-1}\mathbf{d} \\ \mathbf{0} \end{pmatrix}, \tag{7}$$

where **L** is a Laplacian operator, and β is a damping coefficient that controls the relative importance of fitting the data versus satisfying the smoothing constraints. The finite difference approximation [*Wang and Anderson*, 1982] for **m** recast into a two-dimensional array, **s**, having column and row indices i and j, implements Laplace's equation

$$\nabla^2\mathbf{s} = 0 \cong \frac{\mathbf{s}_{i-1,j} - 2\mathbf{s}_{i,j} + \mathbf{s}_{i+1,j}}{(\Delta x)^2} + \frac{\mathbf{s}_{i,j-1} - 2\mathbf{s}_{i,j} + \mathbf{s}_{i,j+1}}{(\Delta y)^2}, \tag{8}$$

where Δx and Δy are the respective along-strike and surface projection of the downdip fault patch dimensions. The matrix **L** is constructed so that the nth row in **L** contains source component coefficients in equation (8) for columns corresponding to the appropriate source

$$L^n = \begin{vmatrix} L^n_{(j-1)\mathrm{nc}+i} = -2\left[(\Delta x)^{-2} + (\Delta y)^{-2}\right] \\ L^n_{(j-1)\mathrm{nc}+(i-1)} = (\Delta x)^{-2} \\ L^n_{(j-1)\mathrm{nc}+(i+1)} = (\Delta x)^{-2} \\ L^n_{(j-2)\mathrm{nc}+i} = (\Delta y)^{-2} \\ L^n_{j\mathrm{nc}+i} = (\Delta y)^{-2} \end{vmatrix}, \tag{9}$$

where L^n is the nth row vector of **L**, and nc is the number of columns in the two-dimensional node matrix **s**. No dislocation sources lie outside the two-dimensional node array, and Dirichlet-type boundary conditions [*Wang and Anderson*, 1982] are applied to **L**.

3. Results

[25] Equation (7) is inverted to obtain solutions for **m**. Only reverse-slip components are considered based on focal mechanisms [*Melbourne et al.*, 1997; *Mendoza and Hartzell*, 1999; *Hutton et al.*, 2001] and the trench-normal convergence direction of the Rivera and North American plates [*DeMets and Wilson*, 1997]. Inversions performed over a range of damping values produce a family of solutions for each model configuration. Although estimated from a common data vector, the dislocation distributions for the six models have different misfits and roughness characteristics. Because of these differences, comparisons between the different dislocation distributions are difficult to assess. The solutions presented here have similar misfits to facilitate a fair comparison between model configurations and to conduct a systematic sensitivity analysis for each of the HIPSHS assumptions. The best solution for model E (in terms of the misfit versus solution roughness tradeoff) has a misfit of $\chi^2 \sim 97$. This is the highest among all the models tested (Figure 4). Solutions for each model are chosen to allow for maximum damping (Laplacian smoothing) while maintaining the misfit threshold of $\chi^2 \sim 97$ for the 33 GPS observations. The DLS method allows for precise approximations of the misfit threshold rather than singular value decomposition and a specified truncated data spectrum [*Hutton et al.*, 2001; *Masterlark et al.*, 2001], which can result in relatively large incremental changes in misfit between singular values. This analysis is limited to comparing solutions having a common misfit ($\chi^2 \sim 97$).

[26] Relaxing the Poisson-solid assumption (model C) gives a solution that allows for the most damping. The solution for the heterogeneous model (model E) tolerates the least amount of damping while maintaining the specified misfit threshold. With the exception of models E (heterogeneous) and F (non-HIPSHS), the maximum slip for the models considered is less than 6 m, in accord with seismogenic and other geodetic results [*Melbourne et al.*, 1997; *Mendoza and Hartzell*, 1999; *Hutton et al.*, 2001]. Qualitatively, the dislocation distributions for models A through D are similar to those determined in other studies, which used HIPSHS models and the same data vector used in this study [*Melbourne et al.*, 1997; *Hutton et al.*, 2001].

[27] The dislocation distributions for the six models are shown in Figure 5 and corresponding GPS displacement predictions are shown in Figure 6. Dislocation sources for all FEMs suggest regions of relatively large slip beneath the epicenter, in a shallower region 80 km northwest of the epicenter, and in a deeper region about 100 km north of the epicenter. The dislocation source $\mathbf{m}_A$, estimated from the HIPSHS FEM (model A), indicates that the greatest slip is located in the region 80 km northwest of the epicenter. Dislocation sources $\mathbf{m}_B$ through $\mathbf{m}_D$ are similar to that of $\mathbf{m}_A$, although the differences become increasingly apparent in $\mathbf{m}_B$ through $\mathbf{m}_D$, respectively. The general features of dislocation source $\mathbf{m}_E$ (heterogeneous) and $\mathbf{m}_F$ (non-HIPSHS) are somewhat different from those of $\mathbf{m}_A$ through

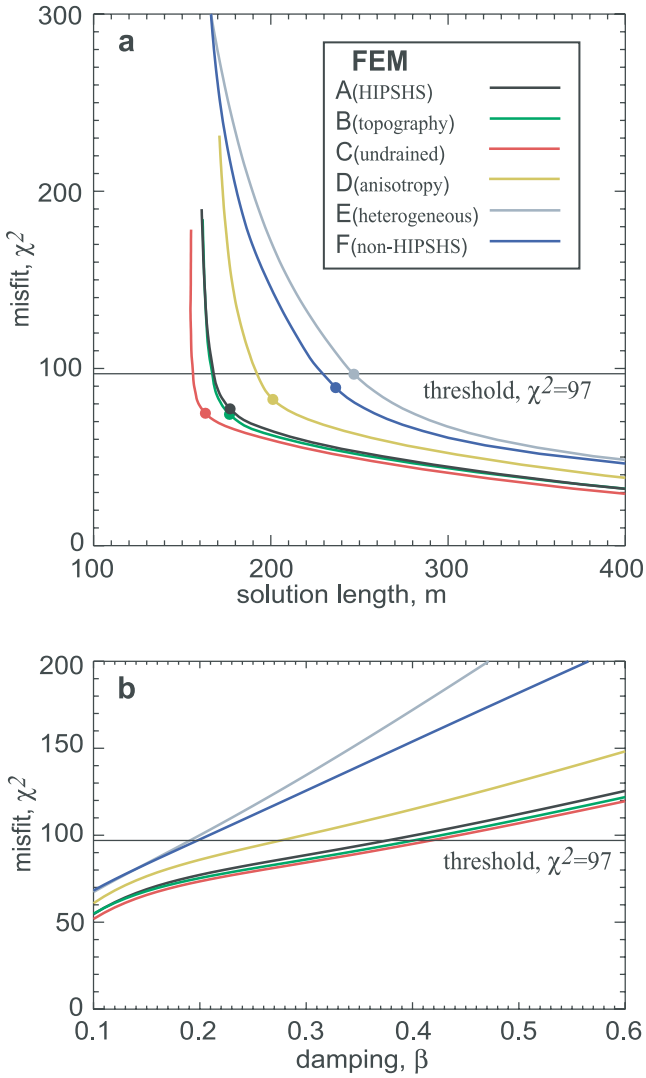

Figure 4. Dislocation model selection. The color code given in the upper right corner applies to both figures in this composite. (a) Solution length (roughness) versus misfit. The solution length is $\Sigma|\mathbf{m}|$. Color-coded circles represent the optimized solutions that would be selected if direct comparisons among the models were not necessary. The horizontal line is the upper limit of the misfit threshold ($\chi^2 = 97$). Solutions intersecting the horizontal line are used to make comparisons among solutions so that they all have similar misfits. The model relaxing the Poisson-solid assumption (model C) has the smallest solution length and can be viewed as the simplest model. The solution from model B (topography) is almost identical to that for model A (HIPSHS). (b) Damping versus misfit. Models C (non-Poisson solid) and E (heterogeneity) tolerate the most and least damping, respectively.

$\mathbf{m}_D$. Dislocation source $\mathbf{m}_E$ suggests that there are two regions having almost equivalent slip and a third substantial slipping region in the northern corner of the fault. The region slightly downdip of the hypocenter dominates $\mathbf{m}_F$. The differences in dislocation distributions vary substantially between $\mathbf{m}_A$ and $\mathbf{m}_E$, and between $\mathbf{m}_A$ and $\mathbf{m}_F$. The dislocation distributions $\mathbf{m}_A$, $\mathbf{m}_E$, and $\mathbf{m}_F$ (HIPSHS, heterogeneous, and non-HIPSHS; respectively) have regions that differ by as much as a few meters, although the deformation prediction misfits from these different dislocation distributions, if applied to their corresponding models, are similar.

[28] The model resolution matrix (**R**) describes how well the predicted model parameters, the dislocation magnitudes in this study, are resolved. This matrix is independent of the data vector and is a function of the data kernel (**G**) and the weighting matrix (**w**) [*Menke*, 1989]. The diagonal elements of **R** indicate how well the dislocation magnitude for each node-pair is resolved. Model parameters are perfectly resolved if **R** is an identity matrix. The absolute values of the model resolution matrix components are arbitrarily improved, at the expense of the estimated parameter variance, by refining the FEM tessellation of the fault region. However, the relative variations in resolution over the entire fault indicate where estimated dislocations are best resolved [*Hutton et al.*, 2001].

[29] Figure 7 displays the diagonal elements of the model resolution matrix for the corresponding dislocations estimated for the non-HIPSHS FEM (model F). Overall, dislocation resolution is poorest along the offshore surface expression of the fault and improves in the downdip direction. Local regions of relatively high resolution occur beneath the GPS sites. The diagonal elements of the resolution matrices for models A through E have similar relative distributions over the fault. The downdip improvement in resolution may explain why the estimated slipping region, determined from GPS data [*Melbourne et al.*, 1997; *Hutton et al.*, 2001; *Masterlark et al.*, 2001], dominating the northwest half of the fault is much deeper than the relatively shallow slip estimated from teleseismic data [*Mendoza and Hartzell*, 1999].

[30] To test this hypothesis, synthetic data for the 11 GPS sites are generated from all models by imposing unit dislocations in a shallow patch measuring 40 × 20 km^2 in trench-parallel and trench-normal directions, respectively (Figure 7). Dislocation distributions are estimated using the inverse method discussed above and the synthetic GPS data vector. None of the models can precisely recover the unit dislocation patch from the synthetic GPS data. Estimated dislocation distributions for all models include a few tens of centimeters in the test patch, although significant portions of the dislocation are severely smeared into the higher resolution areas along the downdip half of the simulated fault. This suggests that the differences in dislocation distributions determined from GPS versus teleseismic data are the result of the geometric relationships of the fault and GPS array versus that of the fault and seismic array. Therefore it is possible that none of the dislocation distributions presented in this paper reasonably approximate the actual slip distribution of the M_w = 8.0 earthquake. Alternatively, the discrepancy between seismogenic and geodetic dislocation distributions may be due to interseismic strain and postseismic deformation contaminating the coseismic GPS data. However, because all FEMs share the same geometric relationships, the relative comparisons between model predictions are valid.

[31] Prediction differences introduced by loading model A ($\mathbf{G}_A$) with the dislocation distribution differences for the other models, $\mathbf{m}_B$ through $\mathbf{m}_F$ (Figures 5g–5k) illustrate the prediction sensitivities to each of the HIPSHS assumptions.

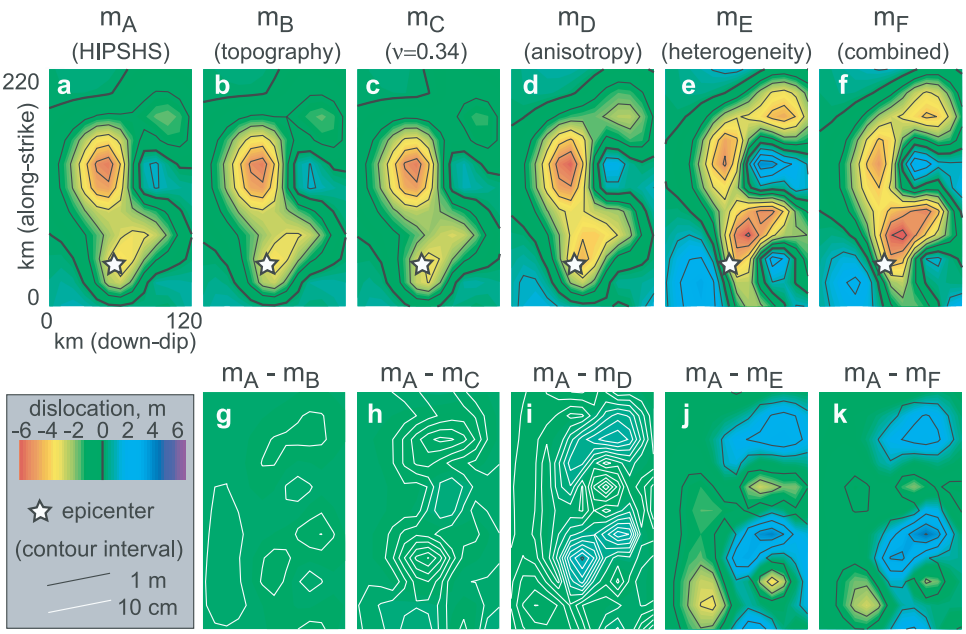

Figure 5. Dislocation distributions. The fault dimensions are labeled in (a). (a–f) Dislocation distributions for models A through F. Dislocation distributions from the six FEMs are shown in the order of increasing difference with respect to model A (HIPSHS). (g–k) Differences between the dislocation source determined for model A and those determined for models that relax the HIPSHS assumptions. Topographic effects are relatively insignificant. The assumption of homogeneous material properties has the greatest influence on the dislocation distribution. The dislocation distributions for models E and F (heterogeneous and non-HIPSHS) differ from that of model A (HIPSHS) by several meters in some portions of the fault.

Prediction errors can be more than an order of magnitude greater than observation measurement uncertainties (Figure 8). Maps of prediction differences are also produced by constructing a synthetic Green's function matrix (**G***) to predict displacements over the entire free surface of the problem domain (Figure 9). Prediction differences much greater than 100% are possible for model A, if loaded with a dislocation distribution other than $\mathbf{m}_A$. For the subduction zone models considered, the respective sensitivities to the HIPSHS assumptions range from slight to severe for the half-space, Poisson-solid, isotropy, and homogeneity assumptions.

[32] Predictions for the GPS displacements are also made by inverting equation (7) using the GPS data and a matrix **G** constructed from analytical solutions for displacement due to a dislocation in an HIPSHS [*Okada*, 1992]. These predictions are within 1σ of those predicted using model A, $\mathbf{G}_A$, and its corresponding dislocation source, $\mathbf{m}_A$ (Figure 8). Although no formal sensitivity analysis of the tessellation density is performed, this excellent agreement between the analytical solution and the FEM approximation verifies the HIPSHS FEM (model A) configuration.

4. Discussion

[33] The usefulness of accurately determined dislocation sources goes beyond predicting static deformation. The static state of a system loaded with a dislocation distribution serves as the initial conditions for transient postseismic phenomena driven by the induced stress and pore fluid pressure distributions. The strain field from a dislocation will produce excess pore fluid pressure in the brittle upper crust [*Wang*, 2000]. If the magnitude and distribution of this excess pore fluid pressure is significant, the subsequent decay of the pressure, via pore fluid flow, will cause measurable, transient poroelastic deformation [*Peltzer et al.*, 1996; *Bosl and Nur*, 1998; *Masterlark et al.*, 2001; *Masterlark and Wang*, 2002]. The deviatoric stresses predicted by a dislocation model drive transient viscoelastic relaxation in the lower crust and upper mantle [*Savage*, 1990; *Pollitz et al.*, 2000; *Masterlark et al.*, 2001; *Pollitz et al.*, 2001; *Masterlark and Wang*, 2002].

[34] Dislocation sources can also predict deformation caused by postseismic afterslip, which occurs downdip from a coseismic rupture [*Scholz*, 1998]. Like viscoelastic relaxation, deviatoric stresses generated by the coseismic slip drive postseismic afterslip. For some fault and slip configurations, displacement prediction patterns for linear viscoelastic relaxation versus afterslip can be difficult to distinguish [*Savage*, 1990]. Numerous studies attribute postseismic deformation to a single mechanism [e.g., *Savage and Svarc*, 1997; *Deng et al.*, 1998; *Hutton et al.*, 2001; *Hsu et al.*, 2002], although it is likely that some combination of driving mechanisms causes transient postseismic deformation. [*Pollitz et al.*, 1998; *Azúa et al.*, 2002; *Masterlark and Wang*, 2002].

[35] The forces driving plate tectonics produce interseismic strain. Stress accumulation along the locked fault and the base of the overriding plate, directly estimated from observed displacement, is a manifestation of this interseismic strain

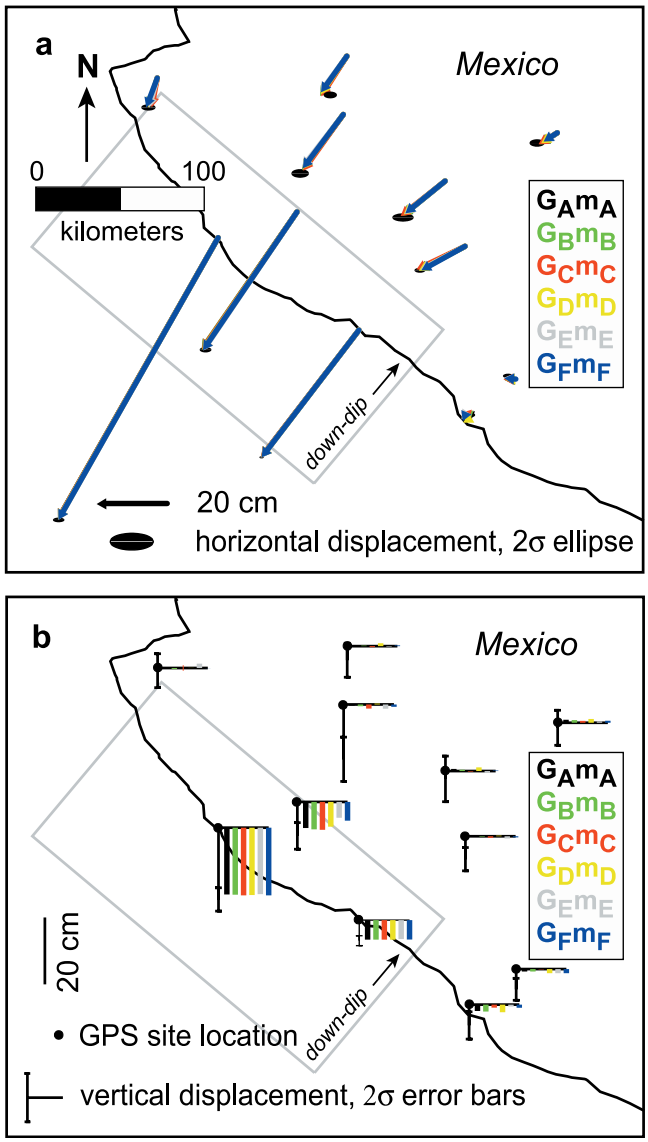

Figure 6. GPS displacement predictions. GPS displacement predictions are calculated for each of the six FEMs, loaded with their respective dislocation distributions. Predictions for each model have misfits of $\chi^2 \sim 97$. The gray rectangle is the surface projection of the fault. The origins of the vectors correspond to the GPS site locations. Color codes for the six models are shown on the boxes on the right side of the figures. (a) Horizontal displacement predictions. Black ellipses are 2σ measurement uncertainties. Prediction differences are difficult to distinguish at this scale. (b) Vertical displacement predictions. Error bars are 2σ measurement uncertainties.

accumulation [*Williams and McCaffrey*, 2001]. Alternatively, the inverse for a coseismic dislocation estimates deformation due to interseismic strain [*Hyndman and Wang*, 1995]. In this case, the stress accumulation is calculated from the spatial derivatives of the deformation for a given set of material property specifications.

[36] Solutions are available for static displacement predictions in the special cases of either a vertically [*Savage*, 1998] or horizontally [*Rodgers et al.*, 2000] layered half-space. Others have gone to great lengths to precisely estimate the geometry of a dislocation source [*Harris and Segall*, 1987; *Cervelli et al.*, 2001; *Hutton et al.*, 2001] in an HIPSHS problem domain. However, the HIPSHS assumptions themselves can have an enormous impact on the dislocation source estimated from observed deformational data. The disadvantage of the FEM method, versus analytical HIPSHS models, is that changing the source geometry requires a new tessellation. Tessellating a problem domain can be a time-consuming process, whereas changing a parameter in an analytical solution is a fast and simple process that lends itself to automated optimization algorithms. However, the development of automated adaptive mesh generating procedures will negate this disadvantage of FEMs.

4.1. Deformation Predictions

[37] All six FEMs, loaded with their respective dislocation distributions, generate deformation predictions that are consistent with the GPS data (Figure 6). This allows a comparison of predictions using the HIPSHS model loaded with the various dislocation distributions to test the sensitivities of deformation predictions on the assumptions in a systematic way. Alternatively, dislocation sources that optimize the tradeoff between misfit and solution length could have been chosen for the individual models. Color-coded circles shown in Figure 4a identify optimal (if this were not a comparative analysis) dislocation distributions. Unfortunately, these optimized solutions share neither misfits nor roughness characteristics and would require some other comparison scheme. The common misfit scheme used in this analysis most directly illustrates that all the models can generate solutions that reasonably match the GPS data. However, interchanging dislocation sources introduces prediction errors directly attributed to the assumptions of the models used to generate the dislocation sources.

[38] For the case of a primarily offshore megathrust event, topographic effects do not contribute significantly to the onshore GPS horizontal displacement predictions (Figure 8). However, prediction errors associated with this assumption can still be significant in offshore regions for all three displacement components (Figures 9a–9c). Sensitivity to topographic effects may be more apparent in configurations where deformational data are available for the region near the surface trace of a rupture, as is the case for the 1999 Landers, California, earthquake [*Massonnet et al.*, 1993; *Freymueller et al.*, 1994], the 1999 Hector Mine, California, earthquake [*Simons et al.*, 2002], the 1999 Chi-Chi, Taiwan, earthquake [*Yang et al.*, 2000], and the 2002 Denali, Alaska, earthquake [*Lu et al.*, 2003].

[39] The Poisson-solid assumption introduces significant prediction errors both on- and offshore (Figures 9d–9f). *Masterlark et al.* [2001] previously demonstrated this result as well as the substantial prediction errors, associated with the Poisson-solid assumption, for transient deformation due to linear viscoelastic relaxation following a dislocation event. Poisson's ratio is 0.25 if Lame's constant and the shear modulus are equivalent. For the case of homogeneous isotropic elastic half-space models of static dislocation, predicted displacements are independent of the shear modulus. Therefore there is no simplification introduced by specifying the equivalency of Lame's constant and the

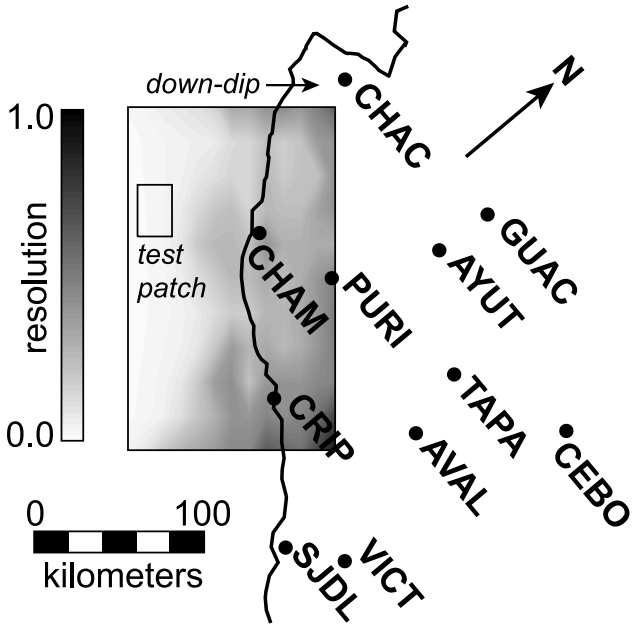

Figure 7. Model resolution. The diagonal components of the model resolution matrix for model F (non-HIPSHS) are plotted in spatial positions for the corresponding dislocation vector (**m**) components. Overall, model resolution is poorest near the offshore surface trace of the fault and progressively improves in the downdip direction, where the fault is beneath a portion of the GPS array. Results are similar for models A through E. The test slip-patch is in a region of poor model resolution and cannot be resolved.

shear modulus [*Converse and Comninou*, 1975]. This equivalency is generally invalid for bulk representations of the crust, particularly for undrained conditions. On the basis of GPS data alone, a homogeneous, isotropic, non-Poisson-solid half-space model is simpler than the HIPSHS model because the dislocation distribution $\mathbf{m}_C$ tolerates the most damping and has the smallest solution length (Figure 4).

[40] The isotropy assumption introduces significant prediction errors both on- and offshore (Figures 9g–9i). For the coastal GPS sites having the largest displacements (CHAM and CRIP), both horizontal and vertical prediction differences associated with isotropy are opposite to those associated with the Poisson-solid assumption (Figure 8). The anisotropic material properties used in this study have compliant axes aligned with the horizontal trench-normal direction. This configuration requires relatively greater

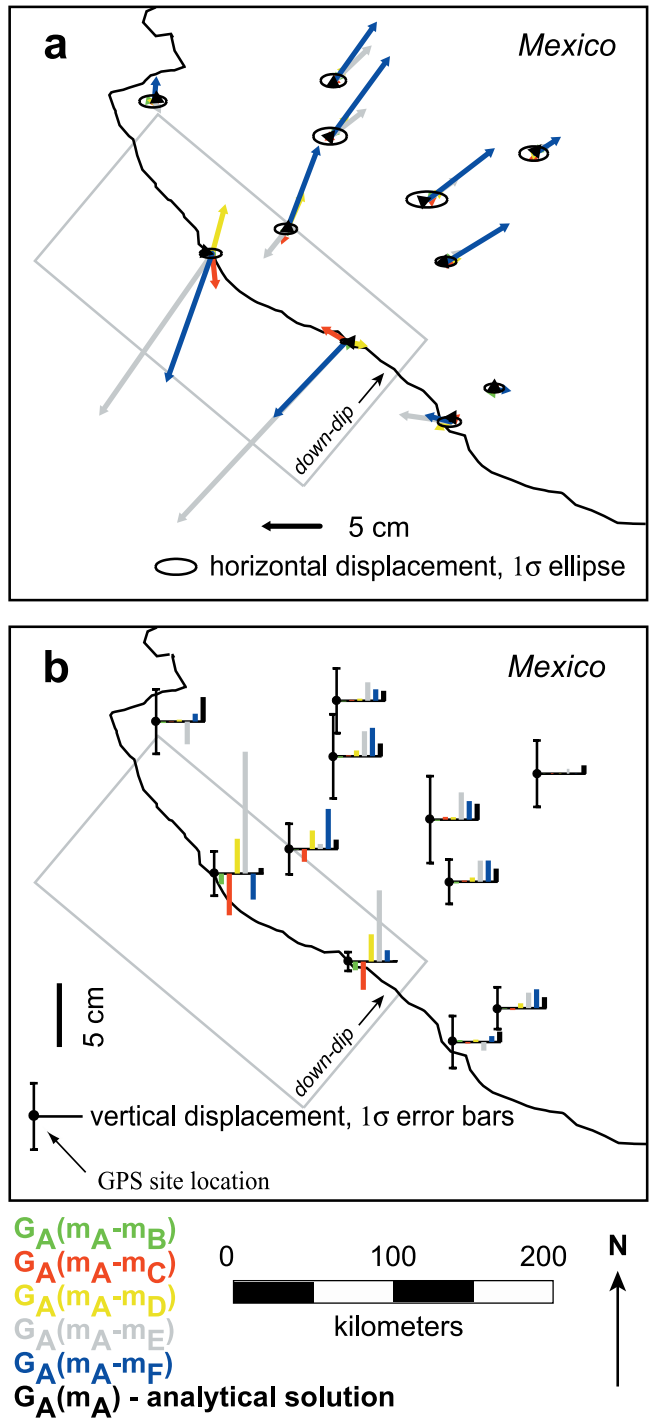

Figure 8. (opposite) GPS displacement prediction sensitivities to HIPSHS assumptions. GPS predictions are made using the HIPSHS model ($\mathbf{G}_A$) loaded with dislocation distributions differences (shown in Figures 5g–5k) to test the GPS displacement prediction sensitivity to each of the HIPSHS assumptions. Prediction differences between $\mathbf{G}_A\mathbf{m}_A$ and an analytical solution (see text) are minimal, suggesting that the FEM tessellation density is sufficient. The gray rectangle is the surface projection of the fault plane. (a) Horizontal prediction differences. With the exception of topographic effects, the sensitivities to the HIPSHS assumptions can be significantly larger than measurement uncertainties. In particular, prediction errors associated with the assumption of a homogeneous material property distribution are more than an order of magnitude greater than GPS measurement uncertainties (gray arrows). Black ellipses, collocated with corresponding GPS sites, are 1σ measurement uncertainties. (b) Vertical prediction differences. The vertical prediction differences are not as systematic as those of the horizontal displacements. Error bars, centered on the GPS site locations, are 1σ measurement uncertainties. Color codes given in the lower left-hand corner apply to Figures 8a and 8b.

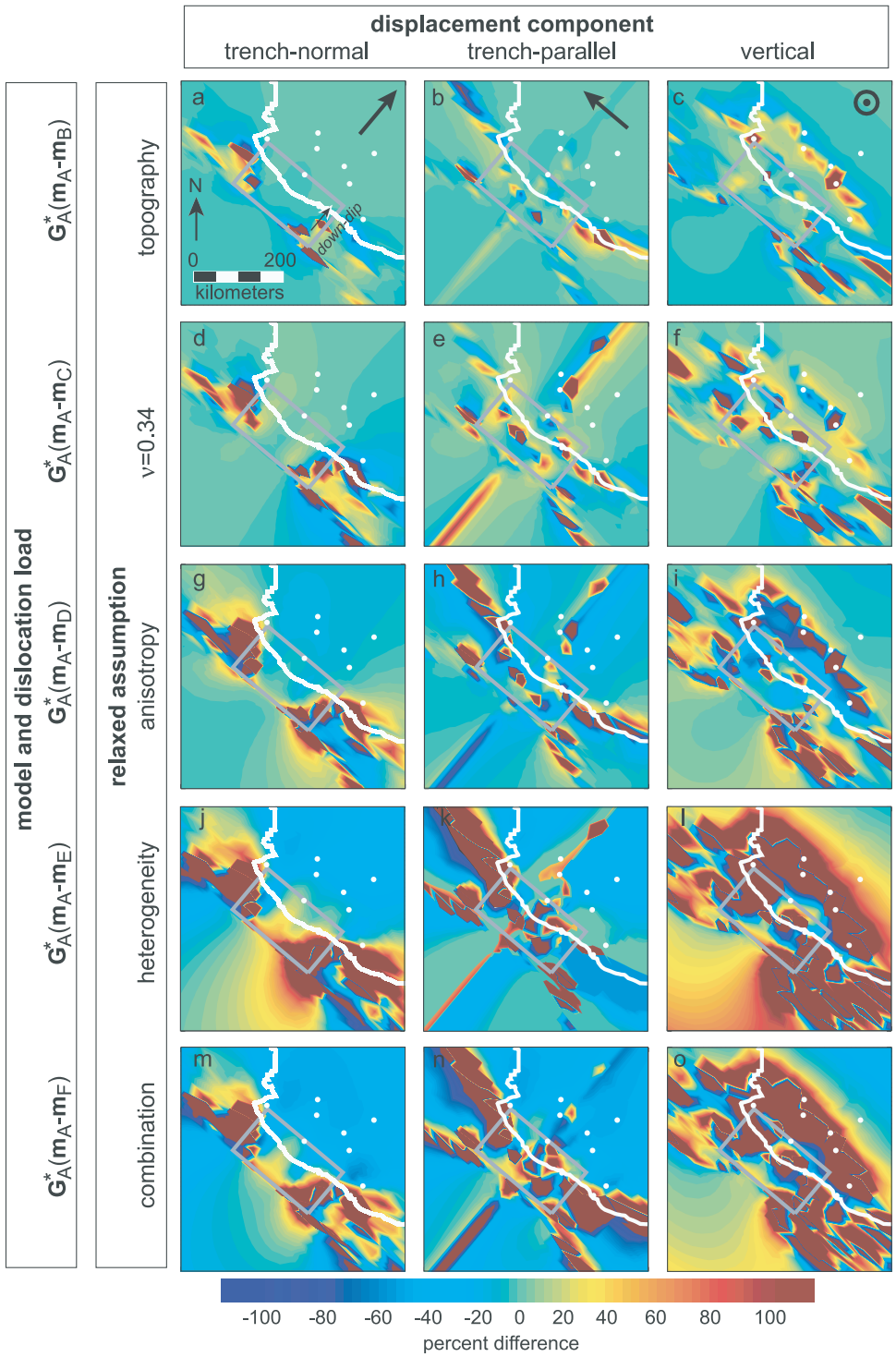

Figure 9. Displacement differences at the free surface. The differences with respect to the HIPSHS model, $\mathbf{G}^*_A$, are loaded with dislocation distribution differences (shown in Figures 5g–5k) to demonstrate the spatial characteristics of the sensitivity to HIPSHS assumptions. The rows correspond to the sensitivity to the various assumptions. The three columns represent displacement components that are trench normal, trench parallel, and vertical. Each assumption can introduce prediction errors greater than 100% in each displacement component. Differing magnitudes among displacement components in a given row indicate rotational components in the prediction errors associated with a given assumption. The magnitudes of the prediction errors, with respect to the individual HIPSHS assumptions, increase from row 1 through row 4. The prediction errors are greatest in row 4, which represents the sensitivity to the assumption of a homogeneous material property distribution. Prediction errors can be much greater than ±100% within horizontal distances of a single fault width. A gray rectangle is the surface projection of the fault. The length scale and north arrow in (a) apply to all figures in this composite. Displacement components are illustrated in the top right corners of Figures 9a–9c. White circles represent GPS site locations.

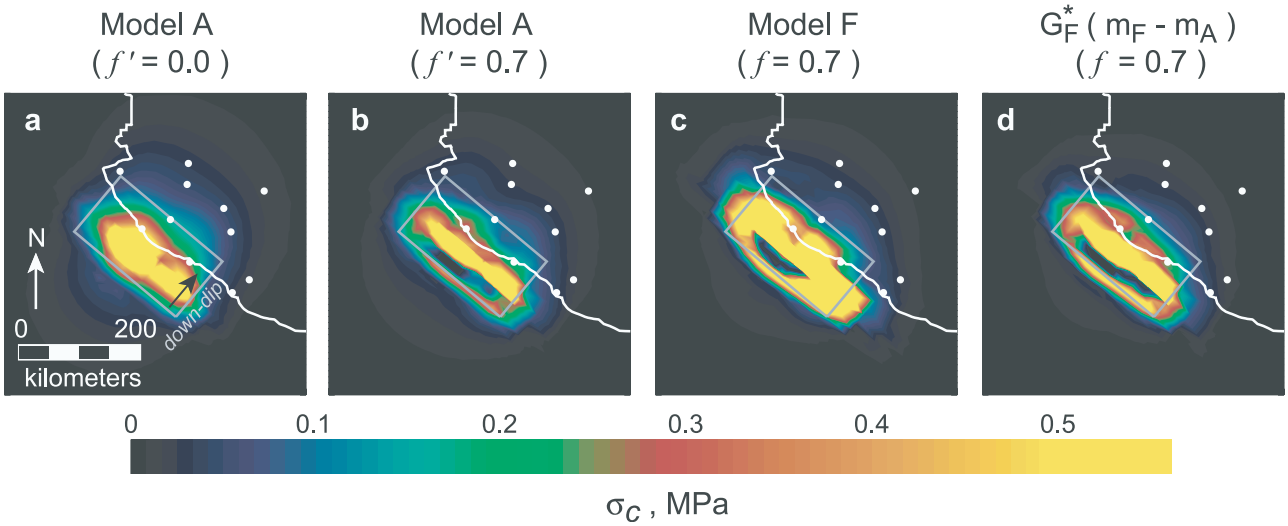

Figure 10. Maximum change in Coulomb stress. Incremental changes in Coulomb stress, σ_C, caused by the M_w = 8.0 earthquake are calculated for optimally oriented faults for a depth of 6 km. The gray rectangle is the surface projection of the fault. White circles are GPS locations. The coastline is shown in white. (a and b) HIPSHS models with apparent coefficients of friction 0.0 and 0.7. (c) Model F loaded with $\mathbf{m}_F$ and having f = 0.7. (d) Model F loaded with the difference between $\mathbf{m}_F$ and $\mathbf{m}_A$. This configuration represents the sensitivity of Coulomb stress predictions to the combined HIPSHS assumptions. Differences near the fault can be more than 1 MPa, an amount that far exceeds what is thought to be the threshold of sensitivity to Coulomb stress (~0.01 MPa).

dislocation magnitudes to produce trench-normal versus trench-parallel displacements. Because of the stress regimes of convergent systems, the isotropy assumption is generally invalid. Although there is a wealth of field and laboratory data emerging that support anisotropic elastic properties in convergent systems (see section 1.2), direct measurements of anisotropy for the Rivera-North America subduction zone are lacking.

[41] The homogeneous assumption introduces the most error in deformation predictions (Figures 8 and 9j–9l). Prediction errors for horizontal displacement are significantly greater than reported measurement uncertainties for all GPS sites (Figure 8). These errors for coastal sites CHAM and CRIP are more than an order of magnitude greater than GPS measurement uncertainties. Prediction errors for vertical displacement, although significant, are less dramatic. *Masterlark et al.* [2001] demonstrated a similar result, along with an estimation of prediction errors associated with subsequent linear viscoelastic relaxation. This suggests that both coseismic and postseismic deformation predictions, generated from models having heterogeneous material property distributions and dislocation sources derived from HIPSHS models [e.g., *Deng et al.*, 1998; *Freed and Lin*, 2001; *Masterlark and Wang*, 2002], contain significant prediction errors. The heterogeneous distribution of material properties associated with a relatively compliant continental crust overriding the relatively stiff subducting oceanic crust in a subduction zone grossly contradicts the homogeneous assumption.

[42] The sensitivity to the homogeneous assumption dominates the prediction errors introduced with the combination of HIPSHS assumptions. Interestingly, horizontal prediction errors associated with the combined suite of HIPSHS assumptions, $\mathbf{G}_A(\mathbf{m}_A - \mathbf{m}_F)$, are much less than

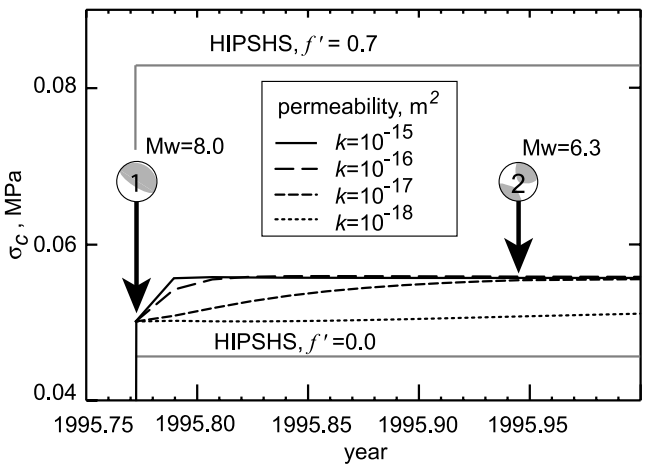

Figure 11. Stress coupling between the M_w = 8.0 and M_w = 6.3 events. Predictions for the evolution of the changes in Coulomb stress (σ_C) for the M_w = 6.3 event fault, caused by the M_w = 8.0 earthquake, are illustrated. Standard methods using static HIPSHS models and apparent coefficients of friction cannot account for the 63-day lag time between events. Predictions for σ_C vary by about 100%, depending upon which apparent coefficient of friction is chosen. The poroelastic model allows for pore fluid pressure recovery in the oceanic crust. The permeability of the oceanic crust controls the speed of pore fluid pressure recovery. If the permeability is greater than 10^{-17} m^2, recovery is too fast to account for the 63-day lag time.

those associated with a heterogeneous material property distribution alone, $\mathbf{G}_A(\mathbf{m}_A - \mathbf{m}_E)$, for the coastal sites CHAM, CRIP, and SJDL. The reverse relationship occurs for the inland GPS sites (Figure 8a). On the basis of the GPS data alone, the dislocation distribution for model F ($\mathbf{m}_F$), which requires none of the HIPSHS assumptions, is simpler than that of the model E ($\mathbf{m}_E$), which allows for a heterogeneous material property distribution (Figure 4). Model F and its corresponding dislocation distribution demonstrate the ability of the FEM method to account for complexities far beyond those allowed in standard HIPSHS models.

[43] On the basis of the GPS data alone, the Poisson-solid assumption is rejected because the optimal dislocation distribution determined for model C is the simplest among the optimal dislocation distributions of the models considered (Figure 4). All the models considered are capable of predicting the data to any given level of precision through the adjustable damping parameter of the inverse method. This general prediction ability, combined with a lack of obvious diagnostic deformation patterns associated with a given HIPSHS assumption, suggests deformational data alone may not be sufficient to require deviations from the HIPSHS assumptions (other than the rejected Poisson-solid assumption as discussed above). However, the well-known structure and mechanical behavior typically associated with subduction zones requires the rejection of all the HIPSHS assumptions. Therefore it is unwise to uphold the HIPSHS assumptions based on GPS data alone. The unnecessary HIPSHS assumptions will introduce significant prediction errors, unless an HIPSHS problem domain truly approximates the natural system.

4.2. Stress Coupling

[44] Causal stress coupling relationships can account for sequences of earthquakes contained in relatively local spatial and temporal regions. Stress coupling calculations are a function of stress and pore fluid pressure, both of which can evolve over time. Transient afterslip, poroelastic effects, and viscoelastic relaxation are responsible for predictable time-dependent changes in quasi-static stress and pore fluid pressure. Changes in Coulomb stress quantify the change in the tendency for frictional slip to occur along a locked, preexisting fault

$$\sigma_C = \sigma_S + f(\sigma_n + P), \tag{10}$$

where σ_C is the incremental change in Coulomb stress, f is a coefficient of friction, σ_S and σ_n are incremental changes in shear stress aligned with the dislocation vector along a fault and fault-normal stress (tension positive), and P is an incremental change in pore fluid pressure [e.g., *Masterlark and Wang*, 2000]. Static (vis-á-vis quasi-static) stress coupling analyses of the causal relationship between earthquakes are applicable for either short times (undrained conditions, negligible viscous relaxation) or long times (drained conditions, negligible deviatoric stresses in the viscous material) following a dislocation [*Wang*, 2000]. Undrained or drained conditions imply either fluid flux = 0 or $P = 0$, respectively. Laboratory experiments on a variety of rocks indicate that the coefficient of friction lies between 0.65 and 0.85 [*Byerlee*, 1978].

[45] Alternatively, changes in Coulomb stress are often calculated using the assumption that fluid pressures are proportional to the fault-normal stress [*Toda et al.*, 2001] rather than the mean-normal stress used in standard poroelastic theory. In this case, equation (10) is modified to

$$\sigma_C = \sigma_S + f'(\sigma_n), \tag{11}$$

where f' is an "apparent coefficient of friction" that is some ambiguous combination of material properties and transient fluid-flow conditions [*Masterlark and Wang*, 2000]. The assumption that pore fluid pressure is proportional to fault-normal stress alone holds only if the fault zone is relatively compliant with respect to the surrounding materials. Equation (11) is typically applied to results from HIPSHS models without deference to fluid-flow conditions or the contradictory heterogeneous distribution of material properties implied by the weak fault zone assumption. Furthermore, drained material property specifications are inconsistent with the inclusion of nonzero pore fluid pressure effects implied by effective coefficients of friction.

[46] FEM predictions of stress and pore fluid pressure can quantify the causal relationship between the M_w = 8.0 earthquake and the subsequent M_w = 6.3 event that occurred 63 days later. The static changes in Coulomb stress are calculated using model A (HIPSHS), typical values for f' [*Harris*, 1998], and equation (11) (Figures 10a and 10b). Coulomb stress predictions calculated with this method for the wedge of continental crust overlying the fault are particularly sensitive to the chosen apparent coefficient of friction and can differ by more than 0.5 MPa. Coseismic changes in Coulomb stress are also calculated using model F, the Coulomb stress formulation in equation (10), and a coefficient of friction (f = 0.7) in accord with laboratory experiments [*Byerlee*, 1978] (Figure 10c). The Coulomb stress predictions from the HIPSHS and non-HIPSHS models using equations (11) and (10), respectively, differ by more than 0.5 MPa in the wedge overlying the fault (Figure 10).

[47] Coulomb stress has been calculated using forward modeling techniques that use mismatched models and dislocation sources. For example, a non-HIPSHS FEM is loaded with a dislocation source estimated from an HIPSHS model that does not match the FEM configuration [*Freed and Lin*, 2001; *Masterlark and Wang*, 2002]. This study simulates the prediction errors in Coulomb stress introduced by a mismatched forward model and dislocation source (Figure 10d). The mismatch introduces prediction errors for Coulomb stress that are much greater than 0.1 MPa in the wedge of continental crust overlying the fault. This suggests that Coulomb stress predictions calculated using mismatched models and dislocation sources can introduce significant errors.

[48] The non-HIPSHS FEM (model F), loaded with its corresponding dislocation distribution, $\mathbf{m}_F$, predicts the evolution of Coulomb stress leading up to the M_w = 6.3 event. Left-lateral dislocation, having strike = 175°, dip = 82°, and rake = 17° (Table 2), consistent with the left-lateral slip along local north-trending faults [*DeMets and Wilson*, 1997], is assumed. The pore fluid pressure in the region initially decreases because of the coseismic load of the M_w = 8.0 earthquake. The recovery of pore fluid pressure causes an evolving increase in Coulomb stress (Figure 11). Permeability of the oceanic crust controls the rate of pore

fluid pressure recovery, and hence the rate of Coulomb stress evolution. The 63-day lag time between the $M_w = 8.0$ and $M_w = 6.3$ events puts an upper limit on the permeability. If the permeability is too high, recovery happens too fast, and the model does not account for the full lag time. Using this logic, the calibrated upper limit on permeability is 10^{-17} m^2, a value in accord with an expected permeability for competent basalt [*Domenico and Schwartz*, 1990; *Ingebritsen and Sanford*, 1998]. None of the stress-coupling models in this study consider other postseismic loading mechanisms such as afterslip and viscoelastic relaxation. The time constant for linear viscoelastic relaxation is on the order of years and will not affect the Coulomb stress significantly during the 63-day postseismic time period. However, the initially rapid postseismic response of either afterslip or power law viscoelastic relaxation could affect the Coulomb stress during the 63-day time period. On the basis of the geometry of the stress-coupling system, both these mechanisms would increase Coulomb stress along the fault of the second earthquake during the 63-day postseismic interval.

5. Conclusions

[49] The implementation of FEMs to generate synthetic Green's functions for static displacement caused by a dislocation source distribution in a non-HIPSHS problem domain is a simple procedure. Although the specific material properties and configurations used in this analysis are debatable, the important point here is that HIPSHS assumptions are not necessary in both forward and inverse models of static and quasi-static deformation.

[50] An overarching caveat for this analysis is that the results and conclusions, other than the demonstrated implementation of FEM-generated synthetic Green's functions, are quantitatively valid only for the specific models and the field situation considered. The relative sensitivities of static deformation predictions to the HIPSHS assumptions, in the order of increasing sensitivity, are half-space (flat free surface), Poisson-solid, elastic isotropy, and homogeneity. Static deformation predictions are relatively insensitive to the topography (an irregular free surface). However, the predictions are very sensitive to the Poisson-solid, isotropic, and homogeneous assumptions, which can introduce prediction errors significantly larger than GPS data uncertainties.

[51] Static stress-coupling predictions calculated from HIPSHS models, using the apparent coefficient of friction formulation, are qualitative at best. The changes in Coulomb stress for the $M_w = 6.3$ event, caused by the previous $M_w = 8.0$ earthquake, calculated with the HIPSHS model can differ by about 100%, depending on the value of the apparent coefficient of friction. Furthermore, the static calculations cannot account for the 63-day lag time between events. Predictions from the non-HIPSHS FEM indicate transient pore fluid pressure recovery following the $M_w = 8.0$ earthquake accounts for the increasing Coulomb stress during the 63-day lag time between events.

[52] Inverse methods using HIPSHS models may estimate precise dislocation distribution parameters; however, the estimations are likely to be inaccurate. Forward modeling predictions using FEMs that do not simulate any or all of the HIPSHS assumptions, loaded with dislocation distributions determined from HIPSHS models, introduce significant displacement prediction errors (with respect to measurement uncertainties) and generate ambiguous Coulomb stress predictions.

[53] **Acknowledgments.** I thank Charles DeMets, David Hart, and Zhong Lu for their encouragement and helpful discussions. Comments from associate editor Teruo Yamashita, insightful reviews by Tomochika Tokunaga and Charles Williams, and proofreading by Pamela Wensing greatly improved this paper. This research was performed in part by the Raytheon and SAIC Corporations under U.S. Geological Survey contract 1434-CR-97-40274 and 03CRCN0001. This research was also supported in part by funding from NASA (NRA-99-OES-10 RADARSAT-0025-0056) and in its early stages by NSF grant EAR-9909321.

References

Azúa, B. M., C. DeMets, and T. Masterlark, Strong interseismic coupling, fault afterslip, and viscoelastic flow before and after the October 9, 1995 Colima-Jalisco earthquake: Continuous GPS measurements from Colima, Mexico, *Geophys. Res. Lett.*, *29*(8), 1281, doi:10.1029/2002GL014702, 2002.

Bawden, G. W., Source parameters for the 1952 Kern County earthquake, California: A joint inversion of leveling and triangulation observations, *J. Geophys. Res.*, *106*, 771–785, 2001.

Bosl, W., and A. Nur, Numerical simulation of postseismic deformation due to pore-fluid diffusion, in *Poromechanics*, edited by J.-F. Thimus et al., pp. 23–28, A. A. Balkema, Brookfield, Vt., 1998.

Bosl, W. J., and A. Nur, Aftershocks and pore fluid diffusion following the 1992 Landers earthquake, *J. Geophys. Res.*, *107*(B12), 2366, doi:10.1029/2001JB000155, 2002.

Byerlee, J., Friction of rocks, *Pure Appl. Geophys.*, *116*, 615–626, 1978.

Cervelli, P., M. H. Murray, P. Segall, Y. Aoki, and T. Kato, Estimating source parameters from deformation data, with an application to the March 1997 earthquake swarm off the Izu Peninsula, Japan, *J. Geophys. Res.*, *106*, 11,217–11,237, 2001.

Cheng, A. H.-D., Material coefficients of anisotropic poroelasticity, *Int. J. Rock Mech. Min. Sci.*, *34*, 199–205, 1997.

Christensen, N. I., Poisson's ratio and crustal seismology, *J. Geophys. Res.*, *101*, 3139–3156, 1996.

Christensen, N. I., L. G. Medaris Jr., H. F. Wang, and E. Jelínek, Depth variation of seismic anisotropy and petrology in central European lithosphere: A tectonothermal synthesis from spinel lherzolite, *J. Geophys. Res.*, *106*, 645–664, 2001.

Cohen, S. C., Numerical models of crustal deformation in seismic zones, *Adv. Geophys.*, *41*, 133–231, 1999.

Converse, G., and M. Comninou, Dependence on the elastic constants of surface deformation due to faulting, *Bull. Seismol. Soc. Am.*, *65*, 1173–1176, 1975.

Currie, C. A., J. F. Cassidy, and R. D. Hyndman, A regional study of shear wave splitting above the Cascadia subduction zone: Margin-parallel crustal stress, *Geophys. Res. Lett.*, *28*, 659–662, 2001.

DeMets, C., and S. Stein, Present-day kinematics of the Rivera plate and implications for tectonics in southwestern Mexico, *J. Geophys. Res.*, *95*, 21,931–21,948, 1990.

DeMets, C., and D. S. Wilson, Relative motions of the Pacific, Rivera, North American, and Cocos plates since 0.78 M_a, *J. Geophys. Res.*, *102*, 2789–2806, 1997.

Deng, J., M. Gurnis, H. Kanamori, and E. Hauksson, Viscoelastic flow in the lower crust after the 1992 Landers, California, earthquake, *Science*, *282*, 1601–1772, 1998.

Domenico, P. A., and F. W. Schwartz, *Physical and Chemical Hydrogeology*, 824 pp., John Wiley, Hoboken, N. J., 1990.

Dragert, H., K. Wang, and T. S. James, A silent slip event on the deeper Cascadia subduction interface, *Science*, *292*, 1525–1528, 2001.

Eberhart-Phillips, D., and W. D. Stuart, Material heterogeneity simplifies the picture: Loma Prieta, *Bull. Seismol. Soc. Am.*, *82*, 1964–1968, 1992.

Escobedo, D., J. F. Pacheco, and G. Suárez, Teleseismic body wave analysis of the October 9, 1995 (M_w = 8.0), Colima-Jalisco, Mexico, earthquake and its largest foreshock and aftershock, *Geophys. Res. Lett.*, *25*, 547–550, 1998.

Freed, A. M., and J. Lin, Delayed triggering of the 1999 Hector Mine earthquake by viscoelastic stress transfer, *Nature*, *411*, 180–183, 2001.

Freymueller, J., N. E. King, and P. Segall, The co-seismic slip distribution of the Landers earthquake, *Bull. Seismol. Soc. Am.*, *84*, 646–659, 1994.

Godfrey, N. J., N. I. Christensen, and D. A. Okaya, Anisotropy of schists: Contribution of crustal anisotropy to active source seismic experiments and shear wave splitting observations, *J. Geophys. Res.*, *105*, 27,991–28,007, 2000.

Harris, R. A., Introduction to special section: Stress triggers, stress shadows, and implications for seismic hazard, *J. Geophys. Res.*, *103*, 24,347–24,358, 1998.

Harris, R. A., and P. Segall, Detection of a locked zone at depth on the Parkfield, California, segment of the San Andreas fault, *J. Geophys. Res.*, *92*, 7945–7962, 1987.

Hartog, R., and S. Y. Schwartz, Subduction-induced strain in the upper mantle east of the Mendocino triple junction, California, *J. Geophys. Res.*, *105*, 7909–7930, 2000.

Holbrook, W. S., T. M. Brocher, U. S. ten Brink, and J. A. Hole, Crustal structure of a transform plate boundary: San Francisco Bay and the central California continental margin, *J. Geophys. Res.*, *101*, 22,311–22,334, 1996.

Hsu, Y.-J., N. Bechor, P. Segall, S.-B. Yu, L.-C. Kuo, and K.-F. Ma, Rapid afterslip following the 1999 Chi-Chi, Taiwan earthquake, *Geophys. Res. Lett.*, *29*(16), 1754, doi:10.1029/2002GL014967, 2002.

Hutton, W., C. DeMets, O. Sanchez, G. Suarez, and J. Stock, Slip kinematics and dynamics during and after the 9 October 1995 M_w = 8.0 Colima-Jalisco earthquake, Mexico, from GPS geodetic constraints, *Geophys. J. Int.*, *146*, 637–658, 2001.

Hyndman, R. D., and K. Wang, The rupture zone of Cascadia great earthquakes from current deformation and the thermal regime, *J. Geophys. Res.*, *100*, 22,133–22,154, 1995.

Ingebritsen, S. E., and W. E. Sanford, *Groundwater in Geologic Processes*, 341 pp., Cambridge Univ. Press, New York, 1998.

Ismaïl, W. B., and D. Mainprice, An olivine fabric database: An overview of upper mantle fabrics and seismic anisotropy, *Tectonophysics*, *296*, 145–157, 1998.

Kaufman, P. S., and L. H. Royden, Lower crustal flow in an extensional setting: Constraints from the Halloran Hills region, eastern Mojave Desert, California, *J. Geophys. Res.*, *99*, 15,723–15,739, 1994.

Lu, Z., T. Wright, and C. Wicks, Deformation of the 2002 Denali fault earthquakes, Alaska, mapped by Radarsat-1 interferometry, *EOS Trans. AGU*, in press, 2003.

Marson-Pidgeon, K., M. K. Savage, K. Glenhill, and G. Stuart, Seismic anisotropy beneath the lower half of the North Island, New Zealand, *J. Geophys. Res.*, *104*, 20,277–20,286, 1999.

Massonnet, D., M. Rossi, C. Carmona, F. Adragna, G. Peltzer, K. Feigl, and T. Rabaute, The displacement field of the Landers earthquake mapped by radar interferometry, *Nature*, *364*, 138–142, 1993.

Masterlark, T., and H. Wang, Poroelastic coupling between the 1992 Landers and Big Bear earthquakes, *Geophys. Res. Lett.*, *27*, 3647–3650, 2000.

Masterlark, T., and H. Wang, Transient stress-coupling between the 1992 Landers and 1999 Hector Mine earthquakes, *Bull. Seismol. Soc. Am.*, *92*, 1470–1486, 2002.

Masterlark, T., C. DeMets, H. F. Wang, O. Sánchez, and J. Stock, Homogeneous vs. realistic heterogeneous subduction zone models: Coseismic and postseismic deformation, *Geophys. Res. Lett.*, *28*, 4047–4050, 2001.

Meissner, R., W. D. Mooney, and I. Artemieva, Seismic anisotropy and mantle creep in young orogens, *Geophys. J. Int.*, *149*, 1–14, 2002.

Melbourne, T., I. Carmichael, C. DeMets, K. Hudnut, O. Sánchez, J. Stock, G. Suarez, and F. Webb, The geodetic signature of the *M*8.0 October 9, 1995 Jalisco subduction earthquake, *Geophys. Res. Lett.*, *24*, 715–718, 1997.

Mendoza, C., and S. Hartzell, Fault-slip distribution of the 1995 Colima-Jalisco, Mexico, earthquake, *Bull. Seismol. Soc. Am.*, *89*, 1338–1344, 1999.

Menke, W., *Geophysical Data Analysis: Discrete Inverse Theory*, *Int. Geophys. Ser.*, vol. 45, 289 pp., Academic, San Diego, Calif., 1989.

Miyazaki, S., J. J. McGuire, and P. Segall, A transient subduction zone slip episode in southwest Japan observed by the nationwide GPS array, *J. Geophys. Res.*, *108*(B2), 2087, doi:10.1029/2001JB000456, 2003.

Nur, A., and J. Walder, Hydraulic pulses in the Earth's crust, in *Fault Mechanics and Transport Properties of Rocks*, edited by B. Evans and T. F. Wong, pp. 461–473, Academic, San Diego, Calif., 1992.

Okada, Y., Internal deformation due to shear and tensile faults in a half-space, *Bull. Seismol. Soc. Am.*, *82*, 1018–1040, 1992.

Pardo, M., and G. Suárez, Shape of the subducted Rivera and Cocos plates in southern Mexico: Seismic and tectonic implications, *J. Geophys. Res.*, *100*, 12,357–12,373, 1995.

Parsons, T., Post-1906 stress recovery of the San Andreas fault system calculated from three-dimensional finite element analysis, *J. Geophys. Res.*, *107*(B8), 2162, doi:10.1029/2001JB001051, 2002.

Peltzer, G., P. Rosen, F. Rogez, and K. Hudnut, Postseismic rebound in fault step-overs caused by pore-fluid flow, *Science*, *273*, 1202–1204, 1996.

Pollitz, F. F., R. Bürgmann, and P. Segall, Joint estimation of afterslip rate and postseismic relaxation following the 1989 Loma Prieta earthquake, *J. Geophys. Res.*, *103*, 26,975–26,992, 1998.

Pollitz, F. F., G. Peltzer, and R. Bürgmann, Mobility of continental mantle: Evidence from postseismic geodetic observations following the 1992 Landers earthquake, *J. Geophys. Res.*, *105*, 8035–8054, 2000.

Pollitz, F. F., C. Wicks, and W. Thatcher, Mantle flow beneath a continental strike-slip fault: Postseismic deformation after the 1999 Hector Mine earthquake, *Science*, *293*, 1814–1818, 2001.

Pritchard, M. E., M. Simons, P. A. Rosen, S. Hensley, and F. H. Webb, Co-seismic slip from the 1995 July 1995 30 M_w = 8.1 Antofagusta, Chile, earthquake as constrained by InSAR and GPS observations, *Geophys. J. Int.*, *150*, 362–376, 2002.

Rodgers, M. J., S. Wen, and L. M. Keer, Surface displacements and energy release rates for constant stress drop slip zones in joined elastic quarter spaces, *J. Geophys. Res.*, *105*, 19,111–19,119, 2000.

Rubin, A. M., and D. Gillard, Aftershock asymmetry/rupture directivity among central San Andreas fault microearthquakes, *J. Geophys. Res.*, *105*, 19,095–19,109, 2000.

Russo, R. M., and P. G. Silver, Trench-parallel flow beneath the Nazca plate from seismic anisotropy, *Science*, *263*, 1105–1111, 1994.

Savage, J. C., Equivalent strike-slip earthquake cycle in half-space and lithosphere-aesthenosphere Earth models, *J. Geophys. Res.*, *95*, 4873–4879, 1990.

Savage, J. C., Displacement field for an edge dislocation in a layered half-space, *J. Geophys. Res.*, *103*, 2439–2446, 1998.

Savage, J. C., and J. L. Svarc, Postseismic deformation associated with the M_w = 7.3 Landers earthquake, southern California, *J. Geophys. Res.*, *102*, 7565–7577, 1997.

Scholz, C. H., Earthquakes and friction laws, *Nature*, *391*, 37–42, 1998.

Simons, M., Y. Fialko, and L. Rivera, Coseismic deformation from the 1999 M_w 7.1 Hector Mine, California, earthquake as inferred from InSAR and GPS observations, *Bull. Seismol. Soc. Am.*, *92*, 1390–1402, 2002.

Singh, S. K., L. Ponce, and S. P. Nishenko, The great Jalisco, Mexico, earthquakes of 1932: Subduction of the Rivera plate, *Bull. Seismol. Soc. Am.*, *75*, 1301–1313, 1985.

Smith, A. T., Jr., Time-dependent strain accumulation and release at island arcs: Implications for the 1946 Nankido earthquake, Ph.D. dissertation, 292 pp., Mass. Inst. of Technol., Cambridge, 1974.

Smith, G. P., and G. Ekström, A global study of P_n anisotropy beneath continents, *J. Geophys. Res.*, *104*, 963–980, 1999.

Tinti, S., and A. Armigliato, A 2-D hybrid technique to model the effect of topography on coseismic displacements: Application to the Umbria-Marche (central Italy) 1997 earthquake sequence, *Geophys. J. Int.*, *150*, 542–557, 2002.

Toda, S., R. S. Stein, and G. King, Coulomb 2.0, earthquake and volcano deformation and stress triggering group, U.S. Geol. Surv. Earthquake Hazards Prog., Menlo Park, Calif., 2001.

Turcotte, D. L., and G. J. Schubert, *Geodynamics: Applications of Continuum Physics to Geological Problems*, 450 pp., John Wiley, Hoboken, N. J., 1982.

Vauchez, A., A. Tommasi, and G. Barruol, Rheological heterogeneity, mechanical anisotropy and deformation of the continental lithosphere, *Tectonophysics*, *296*, 61–68, 1998.

Wald, D. J., and R. W. Graves, Resolution analysis of finite fault source inversion using one- and three-dimensional Green's functions: 2. Combining seismic and geodetic data, *J. Geophys. Res.*, *106*, 8767–8788, 2001.

Wald, D. J., and T. H. Heaton, Spatial and temporal distribution of slip for the 1992 Landers, California, earthquake, *Bull. Seismol. Soc. Am.*, *84*, 668–691, 1994.

Wang, H. F., *Theory of Linear Poroelasticity: With Applications to Geomechanics*, 287 pp., Princeton Univ. Press, Princeton, N. J., 2000.

Wang, H. F., and M. P. Anderson, *Introduction to Groundwater Modeling: Finite Difference and Finite Element Methods*, 237 pp., Academic, San Diego, Calif., 1982.

Wang, K., and J. He, Mechanics of low-stress forearcs: Nankai and Cascadia, *J. Geophys. Res.*, *104*, 15,191–15,205, 1999.

Williams, C. A., and R. McCaffrey, Stress rates in the central Cascadia subduction zone inferred from an elastic plate model, *Geophys. Res. Lett.*, *28*, 2125–2128, 2001.

Williams, C. A., and G. Wadge, An accurate and efficient method for including the effects of topography in three-dimensional elastic models of ground deformation with applications to radar interferometry, *J. Geophys. Res.*, *105*, 8103–8120, 2000.

Yang, M., R. J. Rau, J. Y. Yu, and T. T. Yu, Geodetically observed surface displacements of the 1999 Chi-Chi, Taiwan, earthquake, *Earth Planets Space*, *52*, 403–413, 2000.

Yang, X., K. M. Fischer, and G. A. Abers, Seismic anisotropy beneath the Shumagin Islands segment of the Aleutian-Alaska subduction zone, *J. Geophys. Res.*, *100*, 18,165–18,177, 1995.

T. Masterlark, U.S. Geological Survey, 47914 252nd Street, Sioux Falls, SD 57198, USA. (masterlark@usgs.gov)